Spectrally resolved fluxes derived from collocated AIRS and CERES measurements and their application in model evaluation: 2. Cloudy sky and band-by-band cloud radiative forcing over the tropical oceans

Xianglei Huang,[1] Norman G. Loeb,[2] and Wenze Yang[3,4]

Received 25 January 2010; revised 3 July 2010; accepted 16 July 2010; published 2 November 2010.

[1] We first present an algorithm for deriving cloudy sky outgoing spectral flux through the entire longwave spectrum from the collocated Atmospheric Infrared Sounder (AIRS) and Cloud and the Earth's Radiant Energy System (CERES) measurements over the tropical oceans. The algorithm is similar to the one described in part 1 of this series of studies: spectral angular dependent models are developed to estimate the spectral flux of each AIRS channel, and then a multivariate linear prediction scheme is used to estimate spectral fluxes at frequencies not covered by the AIRS instrument. The entire algorithm is validated against synthetic spectra as well as the CERES outgoing longwave radiation (OLR) measurements. Mean difference between the OLR estimated in this way and the collocated CERES OLR is 2.15 W m^{-2} with a standard deviation of 5.51 W m^{-2}. The algorithm behaves consistently well for different combinations of cloud fractions and cloud-surface temperature difference, indicating the robustness of the algorithm for various cloudy scenes. Then, using the Geophysical Fluid Dynamics Laboratory AM2 model as a case study, we illustrate the merit of band-by-band cloud radiative forcings (CRFs) derived from this algorithm in model evaluation. The AM2 tropical annual mean band-by-band CRFs generally agree with the observed counterparts, but some systematic biases in the window bands and over the marine-stratus regions can be clearly identified. An idealized model is used to interpret the results and to explain why the fractional contribution of each band to the broadband CRF is worthy for studying: it is sensitive to cloud height but largely insensitive to the cloud fraction.

Citation: Huang, X., N. G. Loeb, and W. Yang (2010), Spectrally resolved fluxes derived from collocated AIRS and CERES measurements and their application in model evaluation: 2. Cloudy sky and band-by-band cloud radiative forcing over the tropical oceans, *J. Geophys. Res.*, *115*, D21101, doi:10.1029/2010JD013932.

1. Introduction

[2] Part 1 of this series of study [*Huang et al.*, 2008] introduced an algorithm of deriving spectral fluxes at 10 cm^{-1} spectral intervals over the entire longwave spectrum from collocated AIRS (Atmospheric Infrared Sounder) and CERES (Cloud and the Earth's Radiant Energy System) clear-sky observations over the oceans. It also used the GFDL AM2 simulation as a case study to demonstrate the merit of such band-by-band clear-sky fluxes in GCM (general circulation model) evaluation. As a natural continuation, in this study we present a similar algorithm for deriving such spectral fluxes and then band-by-band fluxes from collocated AIRS and CERES cloudy sky observations over the tropical oceans. The merits of spectral fluxes in model evaluations have already been discussed and demonstrated by *Huang et al.* [2006, 2008]. While both studies dealt with the clear-sky band-by-band fluxes, even more meaningful are the band-by-band cloud radiative forcings (CRFs) (i.e., the differences between clear-sky and all-sky fluxes over each individual bands). (The "band" in "band-by-band" refers to the band with a band width on the order of magnitude of 100 cm^{-1}, for example, those bands used in GCM longwave radiation schemes.) Wien's displacement law indicates that the peak of blackbody radiation shifts toward the lower frequency when the temperature decreases. Therefore, absolute amount of cloud emission over any given band is sensitive to its cloud top temperature, as is the fractional contribution to the longwave broadband cloud emission. Moreover, the spectrally dependent extinction

[1]Department of Atmospheric, Oceanic, and Space Sciences, University of Michigan, Ann Arbor, Michigan, USA.
[2]Radiation and Climate Branch, NASA Langley Research Center, Hampton, Virginia, USA.
[3]Hunter College, City University of New York, New York, New York, USA.
[4]Now at Cooperative Institute for Climate and Satellites, Earth System Science Interdisciplinary Research Center, University of Maryland, College Park, Maryland, USA.

Copyright 2010 by the American Geophysical Union.
0148-0227/10/2010JD013932

Table 1. Discrete Intervals of Precipitable Water (*pw*), Cloud Fraction (*f*), Surface-Cloud Temperature Difference (ΔT_{sc}), and Surface Skin Temperature (T_s) Used by CERES Longwave ADMs Under Cloudy Conditions Over the Ocean, Land, and Desert[a]

pw (cm)	*f*	ΔT_{sc} (K)	T_s (K)
0–1	0.001–0.5	<−15	<275
1–3	0.5–0.75	−15 to 85 every 5k	275 to 320 every 5k
3–5	0.75–0.999	> 85	>320
>5	0.999–1.0		

[a]Adapted from Table 4 of *Loeb et al.* [2005].

coefficients of liquid and ice clouds are generally different and gradually vary from one band to another. Therefore, band-by-band CRFs contain much more information than the broadband CRF. Moreover, it is the contributions from water vapor and temperature (which are tightly coupled to each other via clear-sky water vapor and lapse-rate feedbacks) and clouds that are ultimately responsible for the needed outgoing longwave fluxes at TOA to balance the net incoming shortwave fluxes. Given the fact that water vapor and clouds have distinctively different spectral absorption features, the band-by-band fluxes and CRFs potentially could be of insightful help in unveiling how the water vapor and clouds interplay with each other to attain such needed OLR variations. As modeling of clouds still is one of the major issues that plague the advance of climate modeling [*Stephens*, 2005; *Bony et al.*, 2006; *Soden and Held*, 2006], various techniques have been applied to diagnose observed and simulated clouds in innovative ways, for example, compositing cloud process based on synoptic conditions [e.g., *Lau and Crane*, 1995, 1997; *Tselioudis et al.*, 2000; *Norris and Iacobellis*, 2005] and applying statistical cloud classifications [e.g., *Jakob et al.*, 2005; *Rossow et al.*, 2005; *Xu et al.*, 2005, 2007, 2008; *Xu*, 2009; *Luo et al.*, 2007; *Zhang et al.*, 2007]. While these techniques focus on extracting coherent spatial information of cloud systems, band-by-band CRFs are aiming at the spectral information of clouds and provide another insightful dimension to understand and diagnose the observed and simulated clouds.

[3] The themes of this study are the spectral and band-by-band cloud radiative forcing, including (1) deriving them in a manner similar to how their broadband counterparts are derived from the ERBE and CERES observations and (2) illustrating the merit of them in GCM model evaluation. The following sections are organized as follows. Section 2 depicts the satellite data sets and the modeling tools. Section 3 describes the algorithm, the validation, and the examination of the error characteristics for different types of cloudy scenes. Section 4 presents the band-by-band CRFs as derived from collocated AIRS and CERES observations in 2004 and a model-observation comparison of the annual mean band-by-band CRFs. An idealized model with one layer of cloud is used in section 4 to interpret the band-by-band CRFs and to illustrate the merit of fractional contribution of each band to the broadband CRF. Discussions and conclusions are then given in section 5.

2. Data Sets, Models, and Algorithms

[4] The satellite data sets and modeling tools used here are identical to those used in part 1 of this study. Therefore, except facts related to cloudy sky observations and related modeling issues, the rest are only briefly summarized and further information is given by *Huang et al.* [2008] and references therein.

2.1. CERES and AIRS and Collocation Strategy

[5] Two identical CERES instruments (FM3 and FM4) are aboard the NASA *Aqua* spacecraft. The instrument field of view (IFOV) of CERES is about 20 km nadir-view footprint on the surface. Only CERES observations from the cross-track scanning mode are used in this study since AIRS always operates in the cross-track scanning mode. CERES fluxes are derived based on unfiltered radiances and corresponding angular distribution models (ADMs) [*Loeb et al.*, 2001, 2003, 2005, 2007]. The CERES data set used in this study is the Aqua-CERES level 2 footprint data product, the Single Satellite Footprint (SSF) TOA/Surface Fluxes and Clouds Edition 2A. *Loeb et al.* [2005] described the scene-type classification and constructions of ADMs in detail. Only a brief summary is given as follows. The CERES SSF algorithm classifies cloudy sky footprints over the oceans in the following ways: cloudy footprints are first stratified into discrete intervals of precipitable water (*pw*, 4 bins) retrieved from SSM/I (Special Sensor Microwave Imager) [*Goodberlet et al.*, 1990], cloud fraction (*f*, 4 bins) as determined from collocated MODIS imagery [*Minnis et al.*, 1998], surface-cloud temperature differences (ΔT_{sc}, 22 bins) as described by *Minnis et al.* [1998], and image-based surface skin temperature (T_s, 11 bins). Detailed definitions of these discrete intervals are summarized in Table 1. In total, 3872 discrete intervals have been defined in this way. In practice, the CERES SSF data that we examined shows that 2008 discrete intervals are enough to describe all possible cloudy sky scenes observed over the oceans. For each discrete interval, a pseudoradiance parameter (ψ) is further defined [*Loeb et al.*, 2005, equation (15)] to depict the combined influences of cloud parameters (i.e., cloud top temperatures, cloud fractions, and cloud emissivities) and surface parameters (i.e., surface temperatures and emissivities) on the TOA outgoing radiances in the absence of gas absorbers,

$$\psi(T_s, T_c, f, \varepsilon_s, \varepsilon_c) = (1-f)\varepsilon_s B(T_s) + \sum_{j=1}^{2}\left[\varepsilon_s B(T_s)\left(1-\varepsilon_{cj}\right) + \varepsilon_{cj} B\left(T_{cj}\right)\right] f_j, \quad (1)$$

in which f_j is the cloud fraction of the jth cloud layer within a scene ($f = f_1 + f_2$), T_{cj} and ε_{cj} are the cloud top temperature and cloud infrared emissivity of the jth layer, respectively, ε_s is the surface infrared emissivity, and $B(T) = \pi^{-1}\sigma T^4$ where σ is the Stefan-Boltzmann constant. Furthermore, for each 3° view zenith angle bin of a given discrete interval, the relationship between radiance (I) and ψ is defined with a predetermined third-order polynomial fit. Hence, radiances can then be integrated over all zenith angles to produce a flux and the anisotropy factor can be directly computed [*Loeb et al.*, 2005]. Using such angular distribution models (ADMs) significantly reduces both the bias and the root-mean-square (RMS) errors of LW TOA flux. *Loeb et al.* [2007] estimated a bias of 0.2–0.4 W m^{-2} and RMS error < 0.7 W m^{-2} for Aqua-CERES regional mean LW TOA flux.

[6] AIRS is also aboard *Aqua* [*Aumann et al.*, 2003]. It is a grating spectrometer recording radiances at 2378 channels across three bands (3.74–4.61 μm, 6.20–8.22 μm, 8.8–15.4 μm) with a resolving power ($\lambda/\Delta\lambda$) of 1200. AIRS scans from −49° to 49° with a nadir-view footprint of 13.5 km on the surface. It provides an unprecedented data source of the outgoing thermal IR spectra with excellent calibration and dense global coverage [*Chahine et al.*, 2006]. In this study we use the AIRS geolocated and calibrated radiances (level 1B). Among the 2378 AIRS channels, only those recommended by the AIRS team for level-2 retrieval purposes are used. AIRS radiances from the near-IR band, 3.74–4.61 μm (2169–2673 cm^{-1}), are not used because of its nearly negligible contribution to the longwave flux. In addition, AIRS data was screened with a strict quality control procedure to exclude possible bad spectra as done by *Huang and Yung* [2005]. As for collocating AIRS and CERES individual observations, the criteria adopted here are identical to *Huang et al.* [2008]; that is, (1) the time interval between AIRS and CERES observations is within 8 s, and (2) the distance between the center of an AIRS footprint and that of a CERES footprint on the surface ($\Delta_{\text{airs-ceres}}$) is less than 3 km. In this study, we analyze the collocated AIRS and CERES cloudy sky observations over the tropical oceans (30°S–30°N) in the entire year of 2004.

2.2. Models

2.2.1. Forward Radiative Transfer Model

[7] A forward radiative transfer model is needed to construct spectral ADMs suitable for the AIRS channels and to estimate spectral fluxes at frequencies not covered by the AIRS instrument, MODTRAN^{TM}-5 version 2 revision11 (hereafter, MODTRAN5) is used here for this purpose. Collaboratively developed by Air Force Research Laboratory and Spectral Sciences Inc. [*Berk et al.*, 2005], MODTRAN5 inherits the flexibility in handling clouds from its predecessors but significantly improves the spectral resolution to as fine as 0.1 cm^{-1}. Comparisons between MODTRAN5 and a line-by-line radiative transfer model, LBLRTM [*Clough and Iacono*, 1995; *Clough et al.*, 2005], showed agreement up to a few percent or better in the thermal IR transmittances and radiances [*Anderson et al.*, 2006]. In this study, synthetic AIRS spectrum is done by convolving the MODTRAN5 output at 0.1 cm^{-1} resolution with the spectral response functions of individual AIRS channels [*Strow et al.*, 2003, 2006].

2.2.2. GFDL AM2

[8] To illustrate the application of band-by-band CRFs in GCM evaluation, we use a version of AM2 (am2p14), the atmospheric GCM developed at NOAA Geophysical Fluid Dynamics Lab (GFDL). AM2 treats cloud quantities such as cloud liquid water, cloud ice amount, and cloud fraction as prognostic variables. The shortwave and longwave radiation parameterizations follow *Freidenreich and Ramaswamy* [1999] and *Schwarzkopf and Ramaswamy* [1999], respectively. The longwave radiation scheme parameterizes radiative fluxes over eight spectral bands. The TOA flux and CRF of each band can be directly evaluated against the counterparts derived from the collocated AIRS and CERES observations. A detailed description of AM2 is given by *Global Atmosphere Model Development Team* [2004]. We run the AM2 model with observed monthly SSTs from 2000 to 2007. Given that the observational analysis focuses on the year of 2004, here only model output in 2004 are analyzed.

3. Algorithm and Validations

3.1. Algorithm

[9] The algorithm is in principle identical to the one depicted in part 1 [*Huang et al.*, 2008], which consists of two steps: (1) constructing a spectrally dependent ADM to convert spectral radiance to spectral flux at each AIRS channel and (2) estimating the spectral fluxes at frequencies not covered by the AIRS instrument.

3.1.1. Spectral ADM for Each AIRS Channel

[10] The centerpiece of spectrally dependent ADM is the spectrally dependent anisotropic factor, defined as

$$R_v(\theta) = \frac{\pi I_v(\theta)}{F_v}, \tag{2}$$

where $I_v(\theta)$ is the TOA upwelling radiance at frequency v along viewing zenith angle θ and F_v is the TOA upwelling spectra flux at the same frequency v. For each predefined scene type, once $R_v(\theta)$ is determined, then spectral flux can be obtained from the measured $I_v(\theta)$. As done with the broadband anisotropic factor in the ERBE and CERES algorithms, the spectral anisotropic factor here is made to be scene dependent. *Mehta and Susskind* [1999] developed an analogous concept, monochromatic and band averaged effective zenith angles, for use in a Rapid Transmittance Algorithm (RTA) that computes OLR as a function of surface and atmospheric conditions derived from satellite observations. These effective band averaged zenith angles, once derived, are assumed to be independent of scene types and used for all situations.

[11] Similar to part 1, ECMWF ERA-40 reanalysis [*Uppala et al.*, 2005] in conjunction with the MODTRAN5 is used to derive $R_v(\theta)$. While CERES clear-sky ADM over the oceans contains only 14 discrete intervals of precipitable water, lapse rate, and surface skin temperature, its cloudy sky ADM contains 2008 out of 3872 discrete intervals as described in section 2.1 and Table 1. Using pseudoradiances in the CERES cloudy sky ADMs adds further computational cost for simulating spectra and deriving R $_v(\theta)$ for each AIRS channel. To make computation affordable while still retaining maximum consistency with the CERES ADMs, following approach is adopted for carrying out the simulation. As in part 1 [*Huang et al.*, 2008], we still use four months of ECMWF data over the tropical oceans (i.e., 2001 October, 2002 January, April, and July). For each month, four 6 hourly ECMWF ERA-40 fields between 60°S–60°N oceans are randomly chosen and then temperature and humidity profiles over each oceanic grid box are categorized according to its precipitable water (pw) and surface skin temperature (T_s). Second, for each possible jointed discrete interval of pw and T_s, 1200 randomly chosen profiles (or all profiles when the total number of profiles in that category is less than 1200) are archived for the next step. Third, for each archived profile, clouds are then specified with varying cloud top height and cloud fraction so that each individual discrete interval of (pw, T_s, f, ΔT_{sc}) is covered. Fourth, for each cloudy profile generated at the previous step, cloud

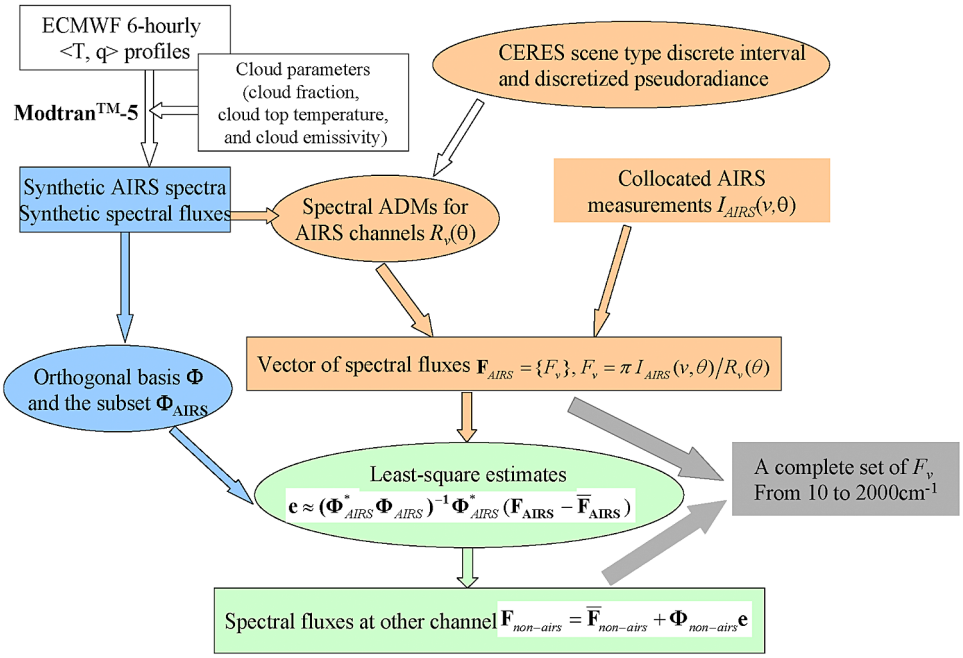

Figure 1. Flowchart illustration of the algorithm for deriving spectral fluxes from the collocated AIRS and CERES measurements. Notations are the same as those defined in section 3 of part 1 of this study [*Huang et al.*, 2008].

emissivity is further varied to produce different pseudoradiance. In original CERES SSF algorithm, ψ varies from 1 to 250 W m^{-2} sr^{-1} with a step size of 1 W m^{-2} sr^{-1}. To save computing time, for each joint discrete interval of (pw, T_s, f, ΔT_{sc}), pseduoradiance is divided into a number of equal intervals from minimum to maximum possible pseudoradiance. When difference between minimum and maximum pseudoradiances (ψ) is small (e.g., discrete intervals for nearly overcast low clouds), only four intervals are used to characterize the variation of ψ. When such difference between minimum and maximum ψ is large (e.g., discrete intervals for nearly overcast high clouds), twenty intervals are used. In between, twelve intervals are used. Last, MODTRAN5 is used to simulate $I_v(\theta)$ and F_v at each AIRS channel and then $R_v(\theta)$ is obtained according to equation (2).

[12] In summary, discretizing pseudoradiance(ψ) adds one more dimension to the original four dimensions of CERES-SSF LW ADM (pw, T_s, f, and ΔT_{sc}) and, by doing so, $R_v(\theta)$ can be estimated for each joint discrete intervals of (pw, T_s, f, ΔT_{sc}, ψ).

3.1.2. Estimating Fluxes Over Frequencies Not Covered by AIRS

[13] Because the grating spectrometer of AIRS does not cover the entire range of longwave spectrum, measures have to be taken to estimate fluxes over spectral ranges without AIRS observations. The method used here is exactly identical to the one described in part 1 [*Huang et al.*, 2008]. In brief, frequency gaps are filled with channels having approximately the same spectral resolutions as the nearest AIRS channels (hereafter, "filled-in" channels). Spectral fluxes over these filled-in channels are then estimated with a multiregression scheme based on the principal component analysis. Parameters in the regression scheme are derived based on the profiles used in section 3.1.1 for each given joint discrete interval of (pw, T_s, f, ΔT_{sc}, ψ). The regression scheme essentially finds the least squares fit of the projections of spectral fluxes at AIRS channels onto the predefined principal components. A chart summarizing the entire algorithm is shown in Figure 1, which is similar to Figure 4 of *Huang et al.* [2008].

3.2. Validations

[14] As in part 1 [*Huang et al.*, 2008], the validation is carried out in two parts. The first part is "theoretical validation," comparing the spectral fluxes derived from the synthetic AIRS spectra to those directly computed from the MODTRAN5, which allows us to assess the entire algorithm without concerning the accuracies in spectroscopy and in the forward model since the MODTRAN5 is deemed as truth through the entire process. The second part uses the algorithm to derive the broadband OLR from the AIRS spectrum and compare it with the collocated CERES OLR, and then characterizing the OLR differences for different combinations of cloud fractions and cloud-surface temperature differences. The second part is more rigorous in the sense that all realistic uncertainties, such as those in spectroscopy, the forward model, and collocation strategies, have been taken into account.

3.2.1. Theoretical Validation

[15] We have examined 32 randomly selected discrete intervals for each of following cases: cloud with inversion boundary layer, low clouds, middle clouds, and high clouds. For each discrete interval, 100 profiles are identified from randomly selected ECMWF ERA-40 6 hourly data (different period from that of the trained data set used in section 3.1). These profiles are then fed into MODTRAN5 to compute

Table 2. Eight Discrete Intervals Used in the Theoretical Validation[a]

	pw (cm)	*f*	ΔT_{sc} (K)	T_s (K)
I1	0–1	0.001–0.5	[−10K, −5K]	[290K, 295K]
I2	0–1	0.001–0.5	[−5K, 0K]	[290K, 295K]
L1	>5	0.999–1.0	[5K, 10K]	[300K, 305K]
L2	>5	0.999–1.0	[10K, 15K]	[300K, 305K]
M1	>5	0.999–1.0	[25K, 30K]	[300K, 305K]
M2	>5	0.999–1.0	[25K, 30K]	[300K, 305K]
H1	>5	0.999–1.0	[55K, 60K]	[300K, 305K]
H2	>5	0.999–1.0	[85K, 90K]	[300K, 305K]

[a]See section 3.2.1 as well as Figures 2 and 3. Symbol definitions are same as in Table 1. I, L, M, and H refer to inverse layer, low cloud, middle cloud, and high cloud, respectively.

OLRs, spectra fluxes, and the synthetic AIRS spectra. Theoretical validation is then done by examining the OLRs and spectral fluxes directly computed from MODTRAN5 (hereafter, computed OLR or spectral fluxes) and the counterparts estimated from synthetic AIRS spectra by the algorithm described in section 3.1 (hereafter, estimated OLR or spectra fluxes). Presented below are summary of eight discrete intervals that have the largest discrepancies between computed and estimated OLR. The detailed information of the eight discrete intervals is tabulated in Table 2. For the rest 24 discrete intervals that we examined, the OLR difference is within ± 5 W m^{-2} and the spectral flux difference is also generally smaller than what is discussed below.

[16] Figure 2 shows differences between directly computed OLR and estimated OLR from synthetic AIRS spectra for three different zenith angels. The mean difference is between −3.66 and 1.11 W m^{-2} for all discrete intervals and zenith angles shown here. The standard deviation is within 2.94 W m^{-2} and maximum difference for any individual case is within ± 12.9 W m^{-2}. For all three enith angles examined here, the largest differences are always seen in the H2 interval as defined in Table 2. The H2 interval is characterized with large amount precipitable water, large cloud-surface temperature contrast, and very high surface temperature (>305K). Such combinations are not frequently seen in ECMWF ERA-40 data. As a result, only around 200 cases from the training data set are identified for the H2 interval and used to develop the algorithm. Therefore, the large difference here for the H2 interval is at least partially due to the fact that the spectral ADM and regression parameters are derived from a very limited set of training profiles.

[17] Figure 3a shows absolute differences between directly computed spectral fluxes over 10 cm^{-1} spectral bin and the estimated ones from synthetic nadir-view AIRS spectra while Figure 3b shows the corresponding relative differences. The largest absolute difference (~± 0.025 W m^{-2}/10 cm^{-1}) is mostly seen over the 650–800 cm^{-1} region of the two discrete intervals featured with inversion boundary layer

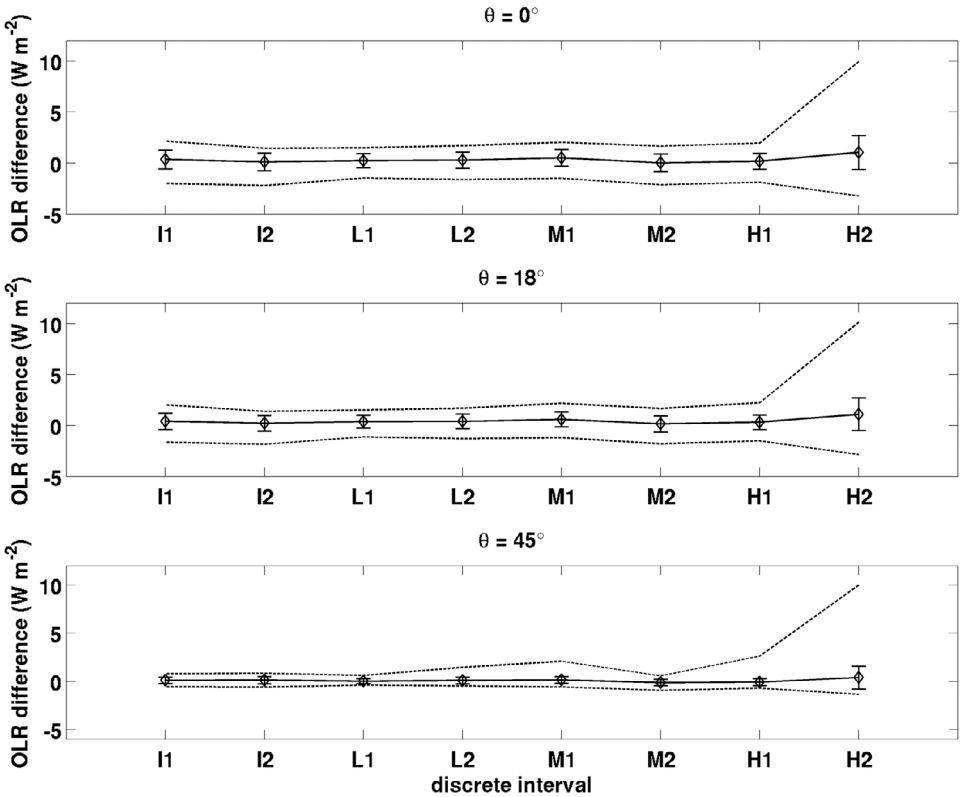

Figure 2. (top) Differences between the OLR predicted from the synthetic nadir-view AIRS spectra and directly computed OLR from MODTRAN^{TM}-5 for eight discrete intervals of CERES cloudy scenes listed in Table 2. The diamond is the mean difference, the error bar shows the mean ± standard deviation, the dashed lines are the maximum and minimum differences. (middle) Same as Figure 2 (top) except a zenith angle of 18°. (bottom) Same as Figure 2 (top) except a zenith angle of 45°.

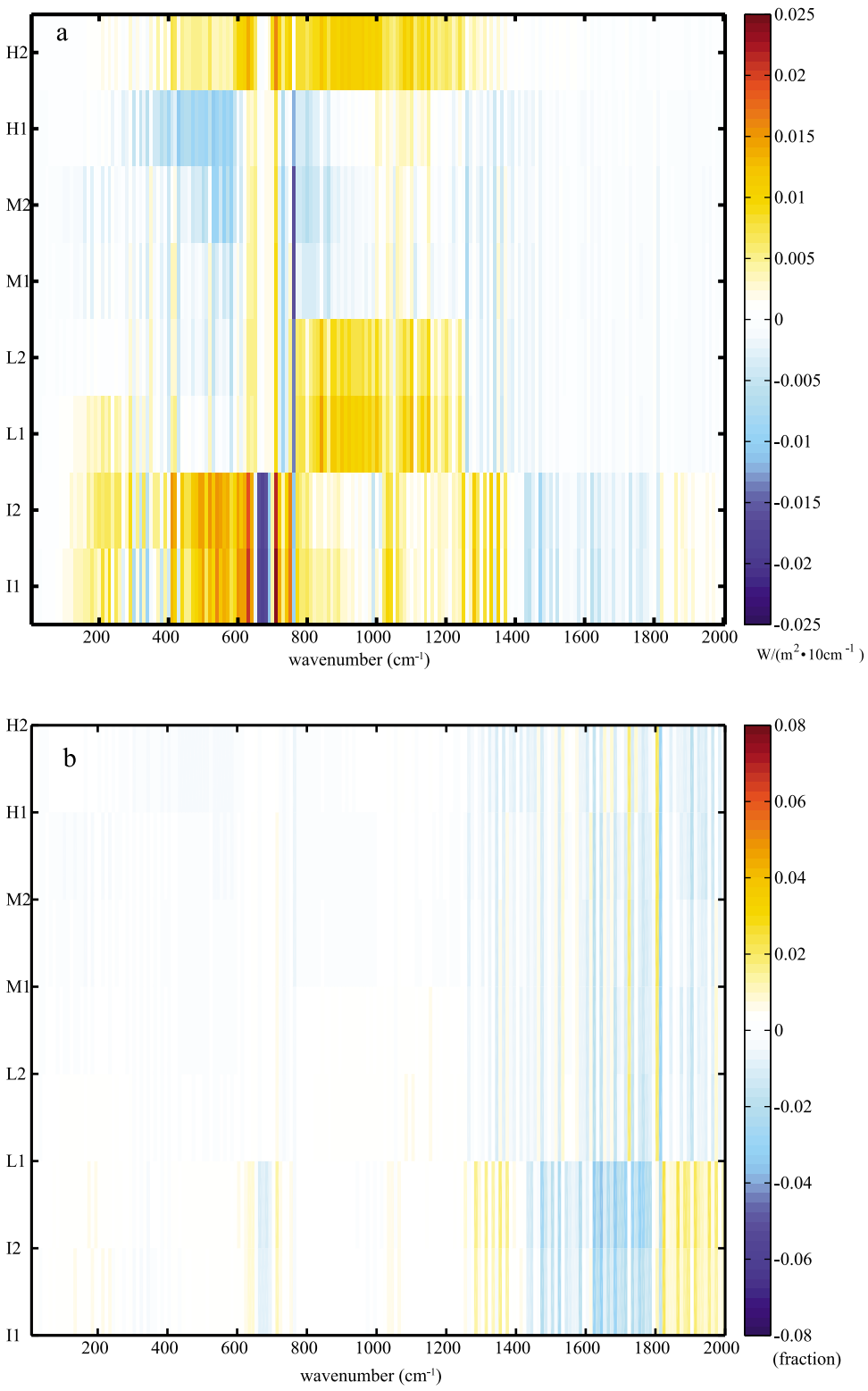

Figure 3. (a) The mean differences between the predicted TOA spectra fluxes based on synthetic AIRS spectra and the directly computed TOA spectral fluxes from MODTRAN^{TM}-5 for each ADM discrete interval. The spectral flux is computed for every 10 cm^{-1} bin from 10 to 2000 cm^{-1}. Ordinate represents the 8 discrete intervals listed in Table 2. The unit of the mean difference is W per m^2 per 10 cm^{-1}. (b) Same as Figure 3a but for the fractional difference.

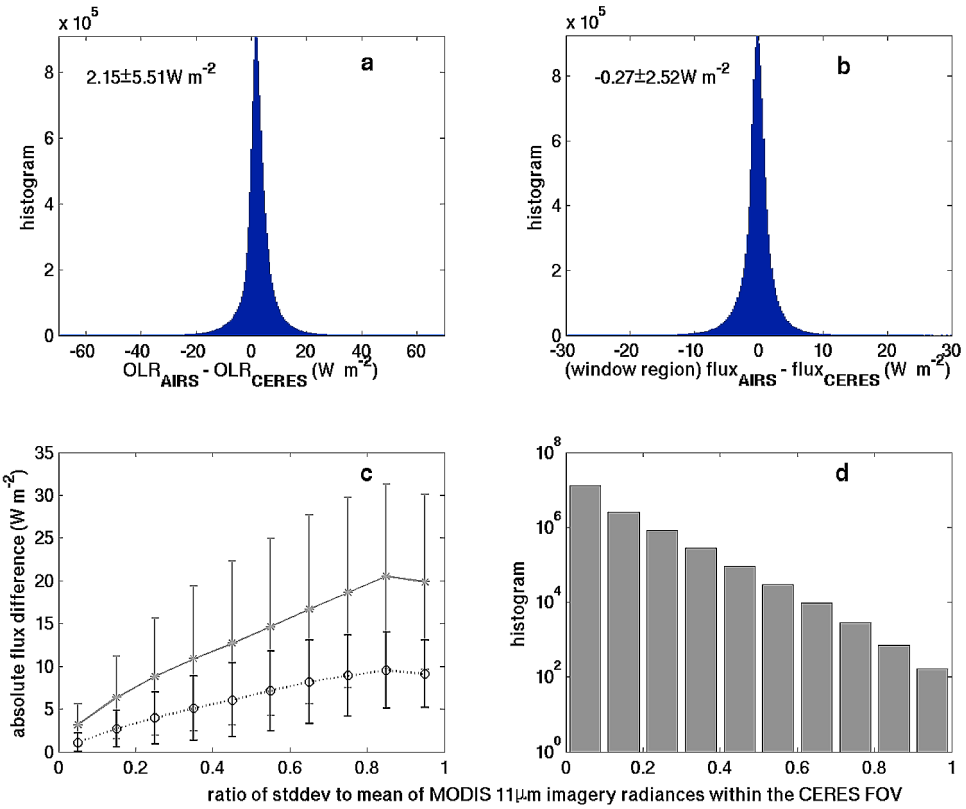

Figure 4. (a) The histogram of differences between OLR estimated from real AIRS spectra and the collocated CERES OLR (OLR_{AIRS}-OLR_{CERES}) over the cloudy tropical oceans in the entire year of 2004; 11.79 million collocated observations are analyzed. Mean and standard deviation of the differences are labeled on the plot. (b) Same as Figure 4a except for the difference between the window channel (8.1–11.8 μm) fluxes estimated from the AIRS spectra and derived in CERES SSF product (WN_{AIRS}-WN_{CERES}). (c) The absolute differences of OLR_{AIRS}-OLR_{CERES} (or WN_{AIRS}-WN_{CERES}) as a function of r_{MODIS}, the ratio of standard deviation-to-mean 1 km MODIS 11 μm imagery radiances within the entire CERES field of view. The bin size of r_{MODIS} is 0.1 with 10 bins from 0.05 to 0.95. The mean OLR differences are denoted by gray stars and the mean window channel flux differences are denoted by black circles. The error bars represents ±1 standard deviation. (d) The histogram of r_{MODIS}. Note the ordinate in logarithm scale. Same bin sizes and bin centers as in Figure 4c are used.

(I1 and I2 intervals); but the corresponding relative difference is indeed small (within 2%, Figure 3b). The largest relative difference is only about ± 3.6% as shown in Figure 3b, which is mostly seen in the water vapor $\nu 2$ band (>1300 cm^{-1}), a band contributing only 2–3% to the broadband OLR. The number of profiles used to derive the algorithm for the I1 and I2 intervals are indeed significantly less than 1200. Such limited samples in the training data set could be a reason why both the largest absolute differences and relative differences tend to happen at the I1 and I2 intervals.

[18] Overall theoretical validations suggest the algorithm itself can reliably estimate spectral fluxes at 10cm^{-1} spectral bin through the entire longwave spectrum. The maximum relative difference for any given 10 cm^{-1} spectral bin is within 3.6% for all discrete intervals that we have examined. These results give us confidence in applying the algorithm to the real AIRS spectra in the next validation step.

3.2.2. Comparisons of Derived OLR With the CERES OLR

[19] For collocated AIRS and CERES cloudy sky observations over the tropical oceans in the entire year of 2004, the AIRS spectra are used to estimate spectral fluxes over every 10 cm^{-1} spectral bin. Broadband OLR estimation is merely a summation of such 10 cm^{-1} spectral fluxes (hereafter, OLR derived in this way is referred as OLR_{AIRS}. This notation is adopted for consistency with notation of *Huang et al.* [2008]. The OLR_{AIRS} is not the OLR product contained in the AIRS level-2 and level-3 data sets). (The OLR product in the AIRS level-2 and level-3 data sets is computed as a function of AIRS retrieved products using the aforementioned RTA for computing OLR [*Mehta and Susskind*, 1999].) In our study OLR_{AIRS} is compared to the collocated OLR from the CERES SSF product (hereafter, OLR_{CERES}). The differences of OLR_{AIRS}-OLR_{CERES} are then further examined for different cloud fractions as well as different surface-cloud temperature differences.

[20] In total 11.79 millions of collocated AIRS and CERES observations over cloudy tropical oceans have been identified for the entire year of 2004. The histogram of differences between OLR_{AIRS} and OLR_{CERES} is shown in Figure 4a, with a mean difference of 2.15 W m^{-2} and a standard deviation of 5.51 W m^{-2}. CERES SSF product also

Table 3. Differences Between OLR Estimated From AIRS Spectra (OLR_{AIRS}) and the Collocated CERES OLR (OLR_{CERES}) for Different Combinations of Cloud Fractions (f) and Cloud-Surface Temperature Difference (ΔT_{sc})[a]

f ΔT_{sc}	<15K	15–40K	>40K
0.001–0.5	1.98 ± 2.04 W m^{-2} (0.6%)	3.93 ± 3.53 W m^{-2} (1.4%)	2.91 ± 4.75 W m^{-2} (1.1%)
0.5–0.75	2.32 ± 3.36 W m^{-2} (0.8%)	4.51 ± 6.18 W m^{-2} (1.7%)	2.18 ± 8.80 W m^{-2} (0.9%)
0.75–0.999	2.02 ± 3.15 W m^{-2} (0.74%)	4.10 ± 6.89 W m^{-2} (1.7%)	−0.12 ± 10.40 W m^{-2} (−0.05%)
0.999–1.0	2.00 ± 2.49 W m^{-2} (0.74%)	5.08 ± 5.70 W m^{-2} (2.2%)	1.58 ± 7.99 W m^{-2} (0.9%)

[a]Mean ± standard deviation of the difference are given for each combination. The fractional mean difference, i.e., $(OLR_{AIRS}\text{-}OLR_{CERES})/OLR_{CERES}$, is given in parentheses.

contains IR window channel (8.1–11.8 μm) flux obtained from its narrow-band radiometer over the window region. For comparison, Figure 4b shows the histogram of differences between window channel flux estimated from AIRS spectra and collocated CERES window channel flux. The mean difference is −0.27 W m^{-2} with a standard deviation of 2.50 W m^{-2}. Both histograms show Gaussian-like distribution; 91.7% of OLR_{AIRS}-OLR_{CERES} differences are within ±10 W m^{-2} and 99.7% of them are within ±27 W m^{-2}.

[21] Though occurrence of large OLR_{AIRS}-OLR_{CERES} difference is rare, the minimum and maximum differences of OLR_{AIRS}-OLR_{CERES} for cloudy scenes could be as large as −66.5 and 58.7 W m^{-2}, respectively (Figure 4a). In contrast, the largest clear-sky OLR_{AIRS}-OLR_{CERES} difference is only around ± 10 W m^{-2} [*Huang et al.*, 2008]. The CERES footprint is larger than the AIRS footprint (at nadir view, ~20 km versus 13 km). Therefore, if cloud distributions within the 20 km CERES footprint vary significantly (i.e., extremely inhomogeneous cloud distribution), cloud properties (cloud fraction and cloud top temperature) observed by CERES can differ from those observed by AIRS. Consequently large bias (either positive or negative) could be introduced for such very inhomogeneous cloud scenes when the CERES ADM is directly applied to the collocated AIRS footprint. This is different from the clear-sky scenes because a clear-sky CERES footprint is generally far more homogeneous. To understand the possible impact of such cloud spatial inhomogeneity within a CERES footprint, we sort the AIRS-CERES differences (for both the OLR and the window channel flux) according to a cloud inhomogeneity index (hereafter denoted as r_{MODIS}) determined from the ratio of the standard deviation-to-mean 1 km MODIS 11 μm radiances within CERES footprints. The mean and standard deviation of MODIS radiances within a CERES footprint are provided in the CERES SSF product. The higher the r_{MODIS} is, the more inhomogeneous the scene is. If the cloud distribution within a CERES footprint is very inhomogeneous, then the cloud amount in the collocated AIRS footprint can be either more or less than the cloud amount of the entire CERES footprint. As a result, the true difference of OLR_{AIRS}-OLR_{CERES} (or window channel flux difference) could either be negative or positive. But the amplitude of the difference (e.g., the absolute value of OLR_{AIRS}-OLR_{CERES}) should be sensitive to the degree of inhomogeneity within the CERES field of view. We thus use the absolute value of OLR_{AIRS}-OLR_{CERES} (or window channel flux difference) here and study how it changes with respect to r_{MODIS}.

[22] Figure 4c shows the mean absolute differences of OLR_{AIRS}-OLR_{CERES} (gray stars) and window channel fluxes (black circles) as a function of r_{MODIS}. The error bars in Figure 4c correspond to ± 1 standard deviation and the bin size of r_{MODIS} is 0.1 with 10 bins centered from 0.05 to 0.95. All 11.79 million of collocated AIRS and CERES cloudy observations over the tropical oceans are used for constructing Figure 4c and 4d. As expected, the smaller r_{MODIS} corresponds to smaller absolute flux differences for both the OLR and the window channel. Figure 4d shows the histogram of r_{MODIS} in logarithmic scale, which indicates a nearly exponential decay of the number of footprints with r_{MODIS}: 77.1% of the cases have r_{MODIS} no more than 0.1 and 99.2% of them have r_{MODIS} no more than 0.4. As showed in Figure 4c, the mean absolute OLR difference for the bin $0.3 \le r_{MODIS} < 0.4$ is 10.9 W m^{-2}. Figures 4c and 4d together indicate that the very inhomogeneous cloud distributions within the CERES footprint are responsible for the very large OLR_{AIRS}-OLR_{CERES} differences shown in Figure 4a, but the frequency of occurrence of such very inhomogeneous scenes is extremely small (0.8% scenes have r_{MODIS} larger than 0.4). Such statistics give us further assurance of applying our algorithm to collocated CERES and AIRS observations.

[23] We further examine the OLR_{AIRS}-OLR_{CERES} differences for different cloud fractions (f) as well as different cloud-surface temperature contrast (ΔT_{sc}). Fraction f is divided into four bins as defined in Table 1. ΔT_{sc} is divided into three bins, approximately representing low clouds, middle clouds, and high clouds. Table 3 summarizes the mean and standard deviation of OLR_{AIRS}-OLR_{CERES} for each possible combination of f and ΔT_{sc}. Changes of mean differences from one combination to another are small and more sensitive to ΔT_{sc} than the cloud fraction. For low clouds and high clouds, the mean differences are clustered around ~2.1 W m^{-2}. For the middle-cloud categories, the mean differences are ~4–5 W m^{-2}. Given the prevalence of mixed-phase clouds for the middle-cloud categories, the relatively larger difference for such categories might be due to different treatment of mixed-phase clouds in our algorithm (which is MODTRAN5 default spectral properties for altostratus) and CERES SSF algorithm. Nevertheless, the relative mean differences are 2.2% or even less for middle clouds and ~1% or less for low and high clouds.

[24] Based on above comparisons, we conclude that the OLR produced by our algorithm agrees well with CERES OLR across different cloud types and cloud fractions. The mean OLR difference is 2.15 W m^{-2} and the standard deviation is 5.51 W m^{-2}. Large OLR differences (e.g., beyond ± 20 W m^{-2}) are mainly due to the very inhomogeneous cloud distribution but the occurrence of such cases are rare (~0.8% when r_{MODIS} is used as indicator of cloud inhomogeneity). Such favorable comparisons give further confidence in using the algorithm to extract spectral fluxes and then band-by-band CRFs.

Table 4. Annual Means of Band-By-Band CRFs Over the Tropical Oceans as Derived From the Collocated AIRS and CERES Observations in 2004 and as Simulated by the AM2 Model Forced by the Observed SST in 2004[a]

	AIRS and CERES Observed CRF (W m^{-2})	AM2 Simulated CRF (W m^{-2})	AM2 Clear-Sky Flux (W m^{-2})
LW broadband	27.45 (100%)	28.13 (100%)	290.88(100%)
0–560 cm^{-1}; > 1400 cm^{-1}	5.36 (19.5%)	5.33 (19.0%)	112.98 (38.8%)
560–800 cm^{-1}	4.18 (15.2%)	3.74 (13.3%)	57.52 (19.8%)
800–900 cm^{-1}	5.11 (18.6%)	5.32 (18.9%)	35.39 (12.2%)
900–990 cm^{-1}	4.24 (15.5%)	4.71 (16.7%)	28.07 (9.7%)
990–1070 cm^{-1}	2.02 (7.0%)	1.68 (6.0%)	12.92 (4.4%)
1070–1200 cm^{-1}	4.31 (15.7%)	5.33 (18.9%)	28.59 (9.8%)
1200–1400 cm^{-1}	2.22 (8.1%)	2.01 (7.2%)	15.43 (5.3%)

[a]The numbers in parentheses are fractional contribution to the longwave broadband CRF. For contrast, the clear-sky OLR and band-by-band fluxes of AM2 tropical annual means are given in the last column, with numbers in parentheses being the fractional contribution to the clear-sky OLR.

[25] Detailed study to quantify the sources of 2.15 W m^{-2} mean difference between OLR_{AIRS}-OLR_{CERES} is beyond the scope of this study. Possible leading candidates are difference in absolute radiometric calibration, biases in scene identification, and differences between CERES ADM and the spectral ADM developed here, and spectroscopy uncertainties in the far IR region. At this time it is not yet possible to separate these contributions one by one. Both AIRS and CERES have carefully designed and in-flight validated calibration procedures. The CERES 2σ absolute calibration uncertainty is 1%, which means ~2.4 W m^{-2} uncertainty for a typical all-sky OLR of 240 W m^{-2}. The AIRS 2σ absolute calibration uncertainty is 0.24% or less. The 2.15 W m^{-2} mean difference shown in Figure 4a is encompassed by the 2σ absolute calibration uncertainty here. Figure 4d suggests the nearly negligible contributions from scene heterogeneity between CERES and AIRS field of view. Furthermore, the very fine discrete intervals of each scene type defined in CERES ADM also help reduce possible biases originated from scene identification.

4. Application in GCM Evaluation

[26] Section 3.2.2 derives band-by-band flux for cloudy sky observations. Together with band-by-band clear-sky flux derived by *Huang et al.* [2008], band-by-band CRFs can then be estimated in the same manner as the broadband CRF derived from ERBE or CERES observations. Then they can be compared to counterparts from GCM simulations. We use the GFDL AM2 model as a case study here. The AM2 model is forced with the observed SST and 3-hourly band-by-band CRFs are archived for the year of 2004, which are then further interpolated onto the times and tracks of AIRS and CERES collocated observations. AM2 longwave radiation scheme has eight bands as listed in Table 4 (in practice the H_2O rotational band and the $v2$ vibrational-rotational band are treated together as Band1, making seven bands in total). Both AIRS and CERES observations happen at fixed local time (LT), around 0130 and 1330 LT. Therefore, daytime and nighttime CRFs are first computed separately and then the daytime and nighttime averages are equally weighted to obtain the overall average. By doing so, bias due to different number of samplings during daytime and nighttime can be minimized. Note no temporal interpolation is employed here. Thus, the average discussed below is the average of two snapshots on the diurnal cycle separated by 12 h (for both observation and model), instead of the true average over the entire diurnal cycle as in the CERES level-3 monthly mean fields. We will focus on the annual means of such band-by-band CRFs as seen from the GFDL AM2 simulations and AIRS and CERES collocated observations.

4.1. Annual Mean CRFs: AIRS and CERES Versus AM2

[27] Figure 5 shows the annual mean spectral CRF over 10 cm^{-1} spectral bins as derived from the AIRS and CERES collocated observation in 2004. The center of CO_2 $v2$ band (~ 650–690 cm^{-1}) is flat, which is expected since this region is sensitive to the emission in the stratosphere. The ozone infrared band is not saturated through the entire atmosphere and hence can be affected by thermal contrast between surface and clouds.

[28] The annual means of band-by-band CRFs and longwave broadband CRF from AIRS and CERES observations are tabulated in Table 4. The fractional contribution of each band to the longwave broadband CRF is also listed. Counterparts from the AM2 simulation are listed in a separate column in Table 4. For comparison, the corresponding tropical means of band-by-band clear-sky fluxes and their

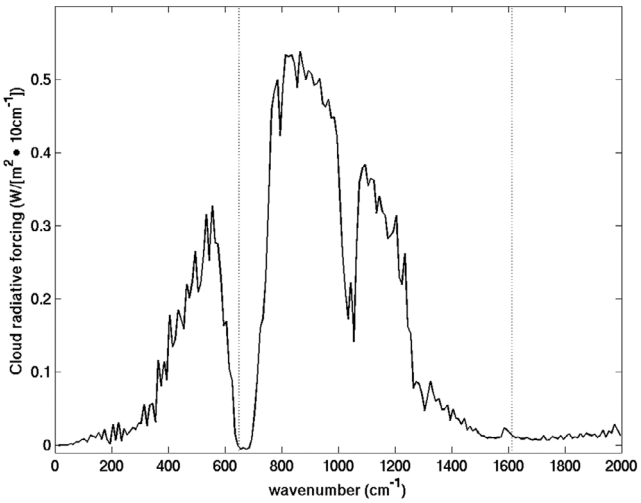

Figure 5. The annual mean spectral CRF at 10 cm^{-1} spectral bin, derived from the collocated AIRS and CERES observations over the tropical oceans for the entire year of 2004. Two vertical dash lines indicate the minimum and maximum frequencies of the AIRS spectra used in this analysis.

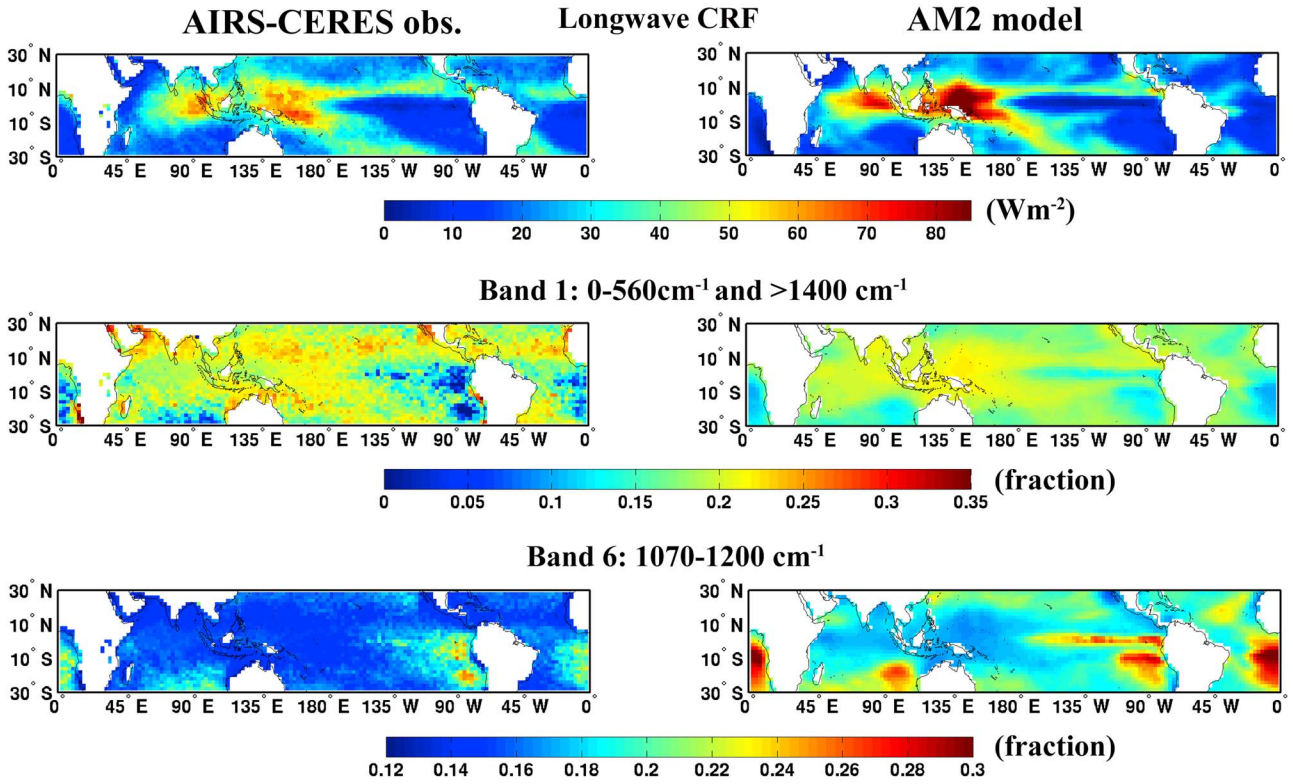

Figure 6. (top) The annual mean longwave broadband CRF (left) from the AIRS and CERES collocated observations and (right) from the AM2 simulation. (middle) The fractional contribution of water vapor rotational band and vibrational $v2$ band to the annual mean longwave CRF. (bottom) Same as Figure 6 (middle) but for 1070–1200 cm^{-1}, a window band.

fractional contributions to clear-sky OLR are listed in the last column of Table 4. The fractional contribution of each band to the broadband CRF is generally not proportional to its fractional contribution to the clear-sky OLR. For example, the H_2O pure rotational band contributes about 38.8% to the clear-sky OLR but only ~19% to the longwave CRF. One window band (1070–1200 cm^{-1}), on the other hand, contributes ~10% to the clear-sky OLR but ~17% to the broadband CRF. Such disproportionality is due to two facts. First, cloud top temperature generally is colder than the surface temperature and, according to the Wien's displacement law, the maximum emission shifts toward lower wave number. Second, spectral dependences of emission and absorption of clouds further contribute to such disproportional change of contributions to clear-sky OLR versus those to longwave CRF.

[29] Comparing the observation and simulation columns in Table 4, AIRS and CERES observation and the AM2 model generally agree with each other on both absolute magnitude of the CRF and the fractional contribution of each band. The spatial distributions of observed and simulated longwave broadband CRF (Figure 6, top) are largely consistent with each other. The largest contribution to broadband longwave CRF comes from the water vapor bands, consisting of ~19.25% of the total longwave CRF. As far as the spatial distribution for the water-vapor-band contributions to the longwave CRF is concerned (Figure 6, middle), observation and simulation agrees on vast area of the tropics, with the AIRS and CERES observations being slightly higher than the AM2 model. The largest discrepancies between AIRS and CERES and AM2 exist in the regions with frequent occurrences of marine stratus, where the fractional contribution in AM2 (~15%) is much higher than that in AIRS and CERES (~5% or less). Therefore, for the water vapor bands, the seemingly agreement on the tropical-averaged fractional contribution between observation and simulation (0–560 cm^{-1} > 1400 cm^{-1} row in Table 4) is indeed due to compensating effect from different geographical regions. Table 4 also shows that the contribution from 800 to 900 cm^{-1}, a window band, to the longwave broadband CRF is only slightly smaller (~18.75%, Table 4) than that from the water vapor rotational band, even the clear-sky flux over this band is less than one third of the water vapor rotational band. Relatively large discrepancy can be seen in another window band (1070–1200 cm^{-1}): observed fractional contribution is 15.7% while the simulated is 18.9%. Spatial maps (Figure 6, bottom) of this band indicate that the simulated contribution of this band is higher than the observed all over the tropical oceans, especially regions featured with frequent coverage of marine stratus. The contrasts in fractional contribution here clearly show the discrepancies between observation and model that cannot be revealed by the broadband CRF comparison alone.

4.2. An Idealized Model for Band-by-Band CRF

[30] An idealized model with one layer of cloud is used here to further interpret the band-by-band CRF results. Sketch of the model is shown in Figure 7a. The fraction of

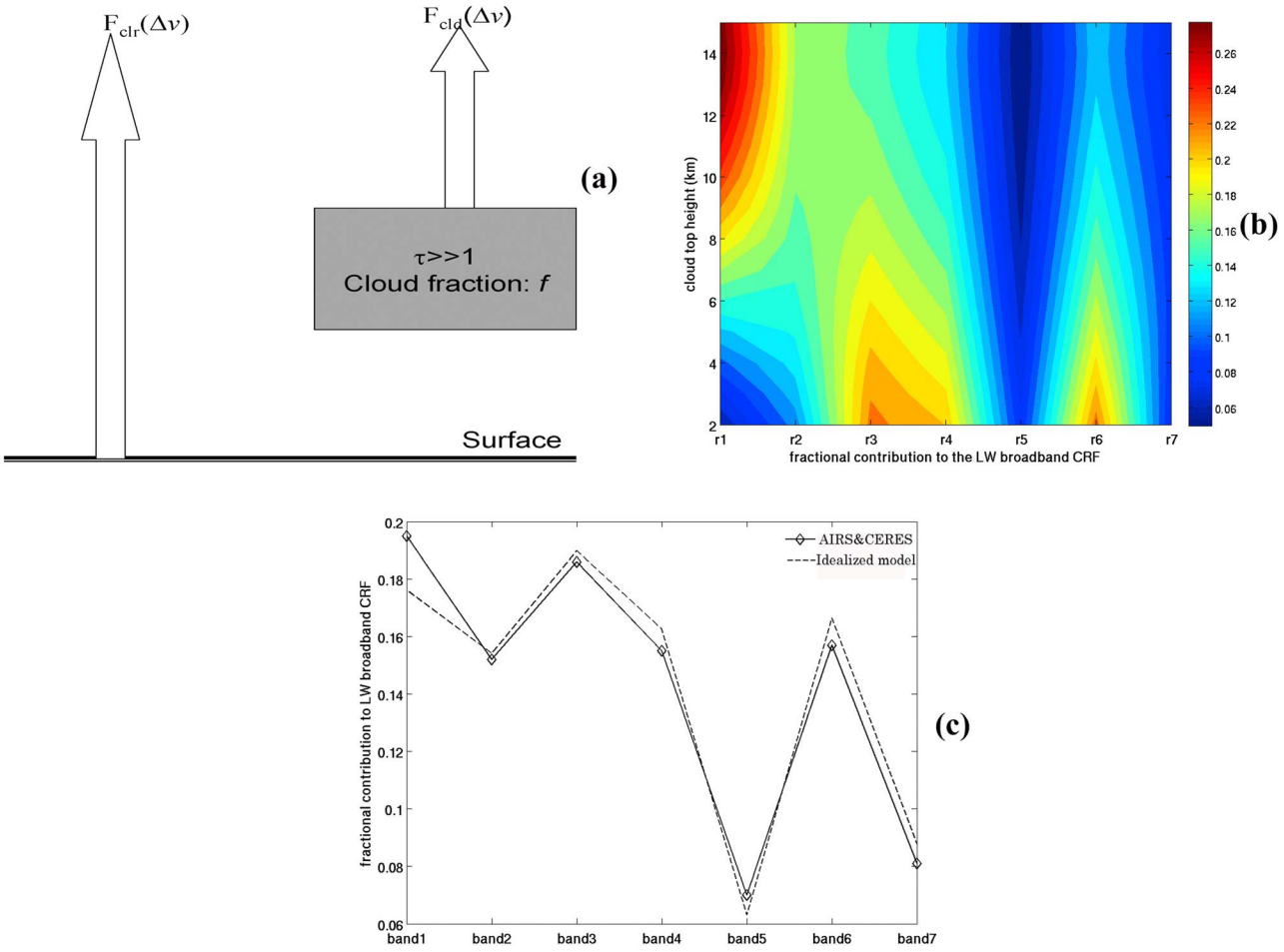

Figure 7. (a) Sketch of the idealized model used in section 4.2. (b) Contours of the fractional contribution of each band to the longwave broadband CRF as the cloud top height changes from 2 km to 15 km in the idealized model. Band 1–7 refers to the bands defined in Table 4 (the bands used in the GFDL AM2 radiation scheme). (c) The fractional contribution of each band to the longwave CRF. Solid line with diamonds is the AIRS and CERES annual mean results as listed in Table 4. Dashed line is result from the idealized model with an optically thick cloud topping at 9.3km, the best fit to the AIRS and CERES curve.

cloudy sky (cloud fraction) is f. Cloud is opaque and MODTRAN5 default cloud spectral features are used in computing fluxes. Typical tropical sounding profiles of temperature, water vapor, and trace gases from *McClatchy et al.* [1972] are used in the calculation. $F_{clr}(\Delta v)$ and $F_{cld}(\Delta v)$ are the clear-sky and cloudy sky fluxes of a band with a bandwidth of Δv, respectively. Then the CRF of this band can be written as

$$CRF(\Delta v) = f[F_{clr}(\Delta v) - F_{cld}(\Delta v)]. \quad (3)$$

[31] The longwave broadband CRF is

$$CRF_{LW} = f[F_{clr_LW} - F_{cld_LW}], \quad (4)$$

where the subscript of LW denotes the longwave broadband quantity (i.e., OLR). The fractional contribution of this band to the CRF_{LW} can then be written as

$$\begin{aligned} r(\Delta v) &= CRF(\Delta v)/CRF_{LW} \\ &= [F_{clr}(\Delta v) - F_{cld}(\Delta v)]/[F_{clr_LW} - F_{cld_LW}]. \end{aligned} \quad (5)$$

[32] While absolute CRF depends on cloud fraction and cloud top height, $r(\Delta v)$ here is not dependent on cloud fraction. For this model, the opaque cloud implies that the outgoing flux over the cloudy sky portion is largely determined by emission from cloud top. Therefore, it can be expected that $r(\Delta v)$ would vary with the cloud top height. The principle of using such ratio to obtain information about cloud top height is similar to the principle behind a well-established IR remote sensing technique, the CO_2 slicing, for obtaining cloud top pressure [e.g., *Smith et al.*, 1974; *McCleese and Wilson*, 1976; *Wylie and Menzel*, 1989], Figure 7b shows such variations of $r(\Delta v)$ for all bands listed in Table 4 when the cloud top height changes from 2 km to 15 km. When the cloud top is low, the maximum contributions are from the window bands since the water vapor bands are mostly sensitive to midtroposphere and upper troposphere and vary little from the clear-sky portion to the cloudy sky portion. As the cloud top height gradually increases, contributions from the window bands become smaller and those from the water vapor bands become larger. This is because the peak of cloud emission shifts

toward lower wave number as cloud top temperature is colder. If the model is used to fit the fractional contributions of AIRS and CERES observations, the best fit is achieved when cloud top height is at 9.3 km (Figure 7c). Figure 7c shows that this highly idealized model can capture the major features of AIRS and CERES band-by-band fractional contribution. The best fit for the AM2 simulation is a cloud top height at 9.5 km (not shown here). Once the cloud top height z_{cld} is determined, the cloud fraction can be obtained by

$$f = \mathrm{CRF_{LW}}/[\mathrm{F_{clr_LW}} - \mathrm{F_{cld_LW}}(z_{cld})], \quad (6)$$

where $F_{cld_LW}(z_{cld})$ is the longwave broadband flux for overcast sky with cloud topping at z_{cld}, and CRF_{LW} is the AIRS and CERES (or AM2) longwave broadband CRF. This would yield a cloud fraction of 24.8% for the AIRS and CERES observation and 25.4% for the AM2 simulation. Note the clouds in this simple conceptual model are clouds that responsible for the LW CRF. For example, marine stratus covers vast area of tropics and subtropics, but it contributes little to the LW CRF is little because it tops at 1 km or even less and thus has little thermal contrast from the surface. As a result, the fitted cloud fraction and cloud top height will contain little contribution from such low clouds. For the same reason, the fitted cloud fraction and cloud top height are better interpreted as the IR effective cloud fraction and cloud top height, which are weighted heavily on high clouds and middle clouds but little on low clouds. These are different from the climatological cloud faction and cloud top height, which equally weight all types of clouds.

[33] The merit of fractional contribution of each band is illustrated by this conceptual model. While the broadband CRF contains two independent macroscopic cloud variables, i.e., cloud fraction and cloud top height, the fractional contributions of individual bands can effectively constrain the cloud top height since it is largely insensitive to the cloud fraction. Cloud fraction can then be estimated once the cloud top height is determined.

5. Conclusion

[34] An algorithm is presented here for deriving spectral flux at 10 cm^{-1} spectral interval through the entire longwave spectrum range from collocated AIRS and CERES cloudy sky observations over the tropical oceans. Its main methodology is identical to the one used by *Huang et al.* [2008]. The algorithm adopts scene type classifications in the CERES-SSF algorithm and builds corresponding spectral ADMs, then employs a multivariate linear regression scheme to estimate fluxes over frequencies not covered by the AIRS instrument. The theoretical validation compares estimated spectral flux from synthetic AIRS data with directly computed spectral flux, indicating maximum fractional difference within ± 3.6%. When comparing OLR derived from real AIRS spectra with the collocated CERES OLR, mean difference is 2.15 W m^{-2} with a standard deviation of 5.51 W m^{-2}. The large differences (e.g., beyond ±27 W m^{-2}) is rare and mostly due to very nonuniform cloud distribution within the collocated CERES footprints, as suggested by the relation between absolute OLR_{AIRS}-OLR_{CERES} differences and r_{MODIS}, an indicator based on MODIS imagery radiance to describe the degree of scene inhomogeneity within the CERES footprint. The statistics of OLR_{AIRS}-OLR_{CERES} differences are similar for different combinations of cloud fractions and cloud types. These facts indicate that the algorithm performs consistently well for all types of cloudy conditions and has no significant bias toward any particular types of clouds.

[35] Based on the spectral fluxes derived for cloudy sky and clear-sky observations, band-by-band CRF is derived for the entire year of 2004. Such band-by-band CRF is then compared to the counterpart from a GCM simulation (the GFDL AM2 model) forced by the observed SST. An idealized model with one layer of cloud is used to illustrate the advantage of band-by-band CRF. The fractional contribution of each band to the LW broadband CRF is insensitive to the cloud fraction but sensitive to cloud top height (equivalently, cloud top temperature). Once the cloud top temperature is estimated from the fractional contributions of different bands, cloud fraction can then be determined by the ratio of the actual broadband CRF to the broadband CRF of overcast situation. As far as the tropical mean band-by-band CRFs are concerned, the AIRS and CERES observation and AM2 simulation generally agree with each other for both the absolute magnitude and fractional contribution of each band. The largest difference (~1 W m^{-2}) is seen in one of the window bands (1070–1200 cm^{-1}). Spatial maps of fractional contribution from the water vapor bands and the window bands both indicate large discrepancies in regions with frequent occurrences of low clouds.

[36] Similar to the discussion in part 1, we acknowledge that AIRS level-2 retrieval products can be used to compute spectral fluxes independently [*Mehta and Susskind*, 1999; *Susskind et al.*, 2003]. There have been a couple of studies focusing on comparing CERES clear-sky OLR and the clear-sky OLR computed from the AIRS retrievals of geophysical parameters [*Dessler et al.*, 2008; *Moy et al.*, 2010]. AIRS level-2 product also contains the clear-sky OLR and all-sky computed from its own algorithm, for observations over both the oceans and the lands. The cloud-clearing approach [*Susskind et al.*, 2003] makes the clear-sky flux computed from quality-controlled AIRS retrieval profiles representing the flux that would have gone to space if the scene were otherwise identical but cloud free, which is consistent with the clear-sky flux used in the definition of cloud radiative forcing. Especially, an encouraging recent study [*Susskind and Molnar*, 2009] indicates that the AIRS level-2 OLR anomalies (both global mean and spatial distribution) agree well with the CERES OLR anomalies.

[37] Our approach is currently limited to the observations over the ocean only. Future work will extend the algorithm to land scenes as well. Meanwhile, if in the future spectral fluxes based on AIRS level-2 retrieved geophysical parameters become available in the AIRS products, it would be meaningful and informative to compare the spectral fluxes derive from such two different approaches, i.e., retrieval-based and radiance-based approaches. The focus of this study is on band-by-band CRFs and its merit in GCM evaluations and, therefore, such extensive study and comparison of OLR and spectral flux products are beyond the scope of this study.

[38] To our knowledge, this is the first time that band-by-band CRFs over the entire longwave spectral range are studied from the combined point of views of satellite observations and GCM modelings. Band-by-band CRFs and fluxes bring additional informative dimensions into the GCM evaluation. To a large extent, diagnostic study using such quantities excludes the nuisance compensating biases from different bands, an issue unavoidable when only broadband quantities are examined. As cloud feedback remains one of key questions in advancing GCM modeling, there is pressing need to decipher modeled biases in CRF and in cloud feedbacks from multitude points of view. Given the intrinsic complexity of cloud feedback mechanism and its intricate connections with radiation, dynamics, and moist processes, orchestrated studies involving different aspects of cloud observations would be required to understand such biases [*Stephens*, 2005]. The feasibility of obtaining band-by-band fluxes and, by extension, band-by-band CRFs from observations, as well as their merits in the GCM evaluation, are shown here and by *Huang et al.* [2008] by using currently available AIRS and CERES observations and the GFDL AM2 model. Such band-by-band quantities are also potentially obtainable from other ongoing or planning hyperspectral measurements (e.g., IASI, CrIS, and CLARREO). Thus, practically band-by-band fluxes and CRFs can play an important role in the orchestrated studies toward a better understanding and simulation of cloud feedback.

[39] **Acknowledgments.** We are greatly indebted to V. Ramaswamy and NOAA GFDL for the generosity of providing computing resources for the AM2 simulation and relevant data analysis. The AIRS data were obtained from NASA GSFC DAAC and the CERES data from NASA Langley DAAC. The ECMWF ERA-40 reanalysis data were obtained from http://data.ecmwf.int/data/d/era40_daily/. One of the authors, X. Huang, thanks L. Strow, G. Aumann, T. Pagano, B. Kahn, S. Souze-Machado, S.Y. Lee, and Z. Luo for valuable discussions and helps on understanding the AIRS data. We also thank two reviewers for their comments. This research is supported partly by NSF AGS CLD program under grant NSF ATM 0755310 and NASA MAP project under grant NNX09AJ46G awarded to the University of Michigan.

References

Anderson, G., et al. (2006), Atmospheric sensitivity to spectral top-of-atmosphere solar irradiance perturbations, using MODTRAN-5 radiative transfer algorithm, *Eos Trans. AGU*, *87*(52), Fall Meet. Suppl., Abstract A11C-05.

Aumann, H. H., et al. (2003), AIRS/AMSU/HSB on the aqua mission: Design, science objectives, data products, and processing systems, *IEEE Trans. Geosci. Remote Sens.*, *41*(2), 253–264, doi:10.1109/TGRS.2002.808356.

Berk, A., et al. (2005), MODTRAN5: A reformulated atmospheric band model with auxiliary species and practical multiple scattering options, *Proc. SPIE Int. Soc. Opt. Eng.*, *5655*, 88.

Bony, S., et al. (2006), How well do we understand and evaluate climate change feedback processes?, *J. Clim.*, *19*, 3445–3482, doi:10.1175/JCLI3819.1.

Chahine, M. T., et al. (2006), Improving weather forecasting and providing new data on greenhouse gases, *Bull. Am. Meteorol. Soc.*, *87*(7), 911–926, doi:10.1175/BAMS-87-7-911.

Clough, S. A., and M. J. Iacono (1995), Line-by-line calculation of atmospheric fluxes and cooling rates: 2. Application to carbon dioxide, ozone, methane, nitrous oxide and the halocarbons, *J. Geophys. Res.*, *100*(D8), 16,519–16,535, doi:10.1029/95JD01386.

Clough, S. A., et al. (2005), Atmospheric radiative transfer modeling: A summary of the AER codes, *J. Quant. Spectrosc. Radiat. Transfer*, *91*(2), 233–244, doi:10.1016/j.jqsrt.2004.05.058.

Dessler, A. E., P. Yang, J. Lee, J. Solbrig, Z. Zhang, and K. Minschwaner (2008), An analysis of the dependence of clear-sky top-of-atmosphere outgoing longwave radiation on atmospheric temperature and water vapor, *J. Geophys. Res.*, *113*, D17102, doi:10.1029/2008JD010137.

Freidenreich, S. M., and V. Ramaswamy (1999), A new multiple-band solar radiative parameterization for general circulation models, *J. Geophys. Res.*, *104*(D24), 31,389–31,409, doi:10.1029/1999JD900456.

Global Atmosphere Model Development Team (2004), The new GFDL global atmosphere and land model AM2–LM2: Evaluation with prescribed SST simulations, *J. Clim.*, *17*, 4641–4673, doi:10.1175/JCLI-3223.1.

Goodberlet, M. A., et al. (1990), Ocean surface wind speed measurements of the Special Sensor Microwave Imager (SSM/I), *IEEE Trans. Geosci. Remote Sens.*, *28*(5), 823–828, doi:10.1109/36.58969.

Huang, X. L., and Y. L. Yung (2005), Spatial and spectral variability of the outgoing thermal IR spectra from AIRS: A case study of July 2003, *J. Geophys. Res.*, *110*, D12102, doi:10.1029/2004JD005530.

Huang, X. L., V. Ramaswamy, and M. D. Schwarzkopf (2006), Quantification of the source of errors in AM2 simulated tropical clear-sky outgoing longwave radiation, *J. Geophys. Res.*, *111*, D14107, doi:10.1029/2005JD006576.

Huang, X. L., W. Yang, N. G. Loeb, and V. Ramaswamy (2008), Spectrally resolved fluxes derived from collocated AIRS and CERES measurements and their application in model evaluation: Clear sky over the tropical oceans, *J. Geophys. Res.*, *113*, D09110, doi:10.1029/2007JD009219.

Jakob, C., et al. (2005), The radiative, cloud, and thermodynamic properties of the major tropical western Pacific cloud regimes, *J. Clim.*, *18*, 1203–1215, doi:10.1175/JCLI3326.1.

Lau, N. C., and M. W. Crane (1995), A satellite view of the synoptic-scale organization of cloud properties in midlatitude and tropical circulation systems, *Mon. Weather Rev.*, *123*(7), 1984–2006, doi:10.1175/1520-0493(1995)123<1984:ASVOTS>2.0.CO;2.

Lau, N. C., and M. W. Crane (1997), Comparing satellite and surface observations of cloud patterns in synoptic-scale circulation systems, *Mon. Weather Rev.*, *125*(12), 3172–3189, doi:10.1175/1520-0493(1997)125<3172:CSASOO>2.0.CO;2.

Loeb, N. G., et al. (2001), Determination of unfiltered radiances from the clouds and the Earth's Radiant Energy System instrument, *J. Appl. Meteorol.*, *40*(4), 822–835, doi:10.1175/1520-0450(2001)040<0822:DOURFT>2.0.CO;2.

Loeb, N. G., et al. (2003), Angular distribution models for top-of-atmosphere radiative flux estimation from the Clouds and the Earth's Radiant Energy System instrument on the Tropical Rainfall Measuring Mission satellite. Part II: Validation, *J. Appl. Meteorol.*, *42*(12), 1748–1769, doi:10.1175/1520-0450(2003)042<1748:ADMFTR>2.0.CO;2.

Loeb, N. G., et al. (2005), Angular distribution models for top-of-atmosphere radiative flux estimation from the Clouds and the Earth's Radiant Energy System instrument on the Terra satellite. Part I: Methodology, *J. Atmos. Oceanic Technol.*, *22*(4), 338–351, doi:10.1175/JTECH1712.1.

Loeb, N. G., et al. (2007), Angular distribution models for top-of-atmosphere radiative flux estimation from the Clouds and the Earth's Radiant Energy System instrument on the Terra satellite. Part II: Validation, *J. Atmos. Oceanic Technol.*, *24*(4), 564–584, doi:10.1175/JTECH1983.1.

Luo, Y. L., et al. (2007), Statistical analyses of satellite cloud object data from CERES. Part III: Comparison with cloud-resolving model simulations of tropical convective clouds, *J. Atmos. Sci.*, *64*(3), 762–785, doi:10.1175/JAS3871.1.

McClatchy, R. A., et al. (1972), Optical properties of the atmosphere, 3rd ed., *AFGRL-72–0497*, 80 pp., Air Force Geophys. Lab., Bedford, Mass.

McCleese, D. J., and L. S. Wilson (1976), Cloud top heights from temperature sounding instruments, *Q. J. R. Meteorol. Soc.*, *102*, 781–790, doi:10.1002/qj.49710243408.

Mehta, A., and J. Susskind (1999), Outgoing longwave radiation from the TOVS Pathfinder Path A data set, *J. Geophys. Res.*, *104*(D10), 12,193–12,212, doi:10.1029/1999JD900059.

Minnis, P., et al. (1998), Parameterizations of reflectance and effective emittance for satellite remote sensing of cloud properties, *J. Atmos. Sci.*, *55*(22), 3313–3339, doi:10.1175/1520-0469(1998)055<3313:PORAEE>2.0.CO;2.

Moy, L. A., R. Knuteson, D. Tobin, H. Revercomb, L. A. Borg, and J. Susskind (2010), Comparison of measured and modeled outgoing longwave radiation for clear-sky ocean and land scenes using coincident CERES and AIRS observations, *J. Geophys. Res.*, *115*, D15110, doi:10.1029/2009JD012758.

Norris, J. R., and S. F. Iacobellis (2005), North Pacific cloud feedbacks inferred from synoptic-scale dynamic and thermodynamic relationships, *J. Clim.*, *18*, 4862–4878, doi:10.1175/JCLI3558.1.

Rossow, W. B., G. Tselioudis, A. Polak, and C. Jakob (2005), Tropical climate described as a distribution of weather states indicated by distinct mesoscale cloud property mixtures, *Geophys. Res. Lett.*, *32*, L21812, doi:10.1029/2005GL024584.

Schwarzkopf, M. D., and V. Ramaswamy (1999), Radiative effects of CH_4, N_2O, halocarbons and the foreign-broadened H_2O continuum: A GCM experiment, *J. Geophys. Res.*, *104*(D8), 9467–9488, doi:10.1029/1999JD900003.

Smith, W. L., et al. (1974), Nimbus 5 sounder data processing system Part I: Measurement characteristics and data reduction procedures, *NOAA Tech. Memo NESS 57*, 99 pp., NOAA, Silver Spring, Md.

Soden, B. J., and I. M. Held (2006), An assessment of climate feedbacks in coupled ocean-atmosphere models, *J. Clim.*, *19*, 3354, doi: 10.1175/JCLI3799.1. (Corrigendum, *J. Clim.*, *19*, 6263, doi:10.1175/JCLI9028.1, 2006)

Stephens, G. L. (2005), Cloud feedbacks in the climate system: A critical review, *J. Clim.*, *18*, 237–273, doi:10.1175/JCLI-3243.1.

Strow, L. L., et al. (2003), Prelaunch spectral calibration of the Atmospheric Infrared Sounder (AIRS), *IEEE Trans. Geosci. Remote Sens.*, *41*(2), 274–286, doi:10.1109/TGRS.2002.808245.

Strow, L. L., et al. (2006), Validation of the Atmospheric Infrared Sounder radiative transfer algorithm, *J. Geophys. Res.*, *111*, D09S06, doi:10.1029/2005JD006146.

Susskind, J., and G. Molnar (2009), Comparison of anomalies and trends of OLR as observed by CERES and computed from geophysical parameters derived from analysis of AIRS/AMSU data, paper presented at 12th CERES Science Team Meeting, NASA Goddard Space Flight Cent., Fort Collins, Co. (Available at http://science.larc.nasa.gov/ceres/STM/2009-11/32_Susskind_1109.pdf)

Susskind, J., C. D. Barnet, and J. M. Blaisdell (2003), Retrieval of atmospheric and surface parameters from AIRS/AMSU/HSB data in the presence of clouds, *IEEE Trans. Geosci. Remote Sens.*, *41*(2), 390–409, doi:10.1109/TGRS.2002.808236.

Tselioudis, G., et al. (2000), Cloud and radiation variations associated with northern midlatitude low and high sea level pressure regimes, *J. Clim.*, *13*, 312–327, doi:10.1175/1520-0442(2000)013<0312:CARVAW>2.0.CO;2.

Uppala, S. M., et al. (2005), The ERA-40 re-analysis, *Q. J. R. Meteorol. Soc.*, *131*, 2961–3012, doi:10.1256/qj.04.176.

Wylie, D. P., and W. P. Menzel (1989), Two years of cloud cover statistics using VAS, *J. Clim.*, *2*, 380–392, doi:10.1175/1520-0442(1989)002<0380:TYOCCS>2.0.CO;2.

Xu, K. M. (2009), Evaluation of cloud physical properties of ECMWF Analysis and Re-Analysis (ERA) against CERES Tropical Deep Convective Cloud Object Observations, *Mon. Weather Rev.*, *137*(1), 207–223, doi:10.1175/2008MWR2633.1.

Xu, K. M., et al. (2005), Statistical analyses of satellite cloud object data from CERES. Part I: Methodology and preliminary results of the 1998 El Niño/2000 La Niña, *J. Clim.*, *18*, 2497–2514, doi:10.1175/JCLI3418.1.

Xu, K. M., et al. (2007), Statistical analyses of satellite cloud object data from CERES. Part II: Tropical convective cloud objects during 1998 El Niño and evidence for supporting the fixed anvil temperature hypothesis, *J. Clim.*, *20*, 819–842, doi:10.1175/JCLI4069.1.

Xu, K. M., et al. (2008), Statistical analyses of satellite cloud object data from CERES. Part IV: Boundary layer cloud objects during 1998 El Niño, *J. Clim.*, *21*, 1500–1521, doi:10.1175/2007JCLI1710.1.

Zhang, Y. Y., S. Klein, G. G. Mace, and J. Boyle (2007), Cluster analysis of tropical clouds using CloudSat data, *Geophys. Res. Lett.*, *34*, L12813, doi:10.1029/2007GL029336.

X. Huang, Department of Atmospheric, Oceanic, and Space Sciences, 2455 Hayward St., University of Michigan, Ann Arbor, MI 48109-2143, USA. (xianglei@umich.edu)

N. G. Loeb, Radiation and Climate Branch, NASA Langley Research Center, Hampton, VA 23681, USA.

W. Yang, Cooperative Institute for Climate and Satellites, Earth System Science Interdisciplinary Research Center, University of Maryland, College Park, MD 20772, USA.